Volume 12
Number 22
21 November 2022
Pages 6613–6922

Catalysis Science & Technology

rsc.li/catalysis

ISSN 2044-4761

ROYAL SOCIETY OF CHEMISTRY

PAPER
Magdalena Jabłońska *et al.*
Selective catalytic reduction of NO_x over micro-/meso-/macroporous Cu-SAPO-34

Catalysis Science & Technology

ROYAL SOCIETY OF CHEMISTRY

PAPER

View Article Online
View Journal | View Issue

Cite this: *Catal. Sci. Technol.*, 2022, **12**, 6660

Selective catalytic reduction of NO_x over micro-/meso-/macroporous Cu-SAPO-34†

Magdalena Jabłońska, *[a] Kinga Góra-Marek, [b] Muhammad Fernadi Lukman,[c] Karolina Tarach,[b] Marko Bertmer, [c] Reinhard Denecke, [d] David Poppitz,[a] Konstantin Marcinowski, [a] Andreas Pöppl[c] and Roger Gläser [a]

Received 1st September 2022,
Accepted 6th October 2022

DOI: 10.1039/d2cy01548j

rsc.li/catalysis

Micro-/meso-/macroporous Cu-containing SAPO-34 was successfully prepared by the post-synthetic modification of a commercial support with diethylamine (DEA). The treatment in disodium ethylenediaminetetraacetate (Na_2H_2EDTA) did not yield a micro-/mesoporous material. The post-synthetic modification of SAPO-34 allows for the introduction of a higher content of copper species (1–2.6 wt%) compared to the unmodified material (0.5 wt%). Cu-SAPO-34_DEA exhibits the highest NO conversion below 250 °C, and the widest activity temperature window to achieve >80% of NO conversion (200–450 °C) during NH_3-SCR-DeNO$_x$. However, the presence of H_2O in the feed was detrimental to all the materials. As evidenced by DR UV-vis and *in situ* XPS, the mobility of copper species and their accumulation in the internal part of SAPO-34 grains appeared with increasing temperature. By employing the rapid scan FT-IR approach, the consecutive reaction steps were identified in the first 300 s of NH_3-SCR-DeNO$_x$ in the presence of H_2O.

1. Introduction

The selective catalytic reduction of NO_x by ammonia (NH_3-SCR) is the most widely and effectively known DeNO$_x$ technology.[1–3] V_2O_5–WO_3, Cu-SSZ-13, and Cu-ZSM-5 are representative catalysts for this reaction. Cu-SSZ-13 and Cu-SAPO-34 have been commercially applied in diesel after-treatment systems due to their improved activity, selectivity and stability.[4–6] Both SSZ-13 and SAPO-34 zeolites have the same chabazite (CHA) framework structure that contains double six-membered ring prisms (D6-MRs) in the large cavities of the structure. Unlike SSZ-13, whose framework is built from aluminosilicate structures, with Si and Al as tetrahedral, the SAPO-34 framework is generated by the substitution of Si in the AlPO structure that was initially formed by P. The hydrothermal synthesis of SAPO-34 utilizes common zeolite structure-directing agents (SDAs) such as TEA (triethylamine), TEAOH (tetraethylammonium hydroxide) or MOR (morpholine), while SSZ-13 synthesis mostly uses a very costly structural directing agent, *N*,*N*,*N*-trimethyl-1-adamantammonium hydroxide (TMAdaOH).[7] Furthermore, in NH_3-SCR-DeNO$_x$, Cu-SAPO-34 is reported to reveal a similar or even higher activity during NO_x removal than Cu-SSZ-13 in a wide range of temperatures (*e.g.*, ref. 8–10). Recently, Jabłońska *et al.*[11] reviewed the preparation procedures, the operating temperature ranges with NO_x reduction activity/by-product formation, and the poisoning and deactivation mechanisms as well as NH_3-SCR-DeNO$_x$ reaction mechanisms over copper-containing SAPO-34. From the data gathered in the review, micro-/mesoporous Cu-SAPO-34 was significantly less extensively investigated compared to conventional catalysts applied in NH_3-SCR-DeNO$_x$. For instance, Liu *et al.*[12] applied a hydrothermal method by using Cu-tetraethylenepentamine (TEPA) and *N*,*N*-diisopropylethylamine (DIPEA) in the preparation of micro-/mesoporous Cu-SAPO-34. In other successful examples, the micro-/mesoporous SAPO-34 was also prepared by using MOR and the long-chain organic compound: $[C_{22}H_{45}–N^+(CH_3)_2–C_6H_{12}–N^+(CH_3)_2–C_6H_{13}]Br_2$ ($C_{22\text{-}6\text{-}6}$–Br_2),[13] or a hard-template method using $CaCO_3$.[14,15] An enhanced activity (compared to conventional Cu-SAPO-34) of the catalyst (>80% NO conversion in the range of 150–500 °C) is attributed to the improved accessibility of reactants to catalytically active sites. Otherwise, in another top-down approach, Rutkowska *et al.*[16] modified commercial SAPO-34 by the use of an aqueous

[a] *Institute of Chemical Technology, Universität Leipzig, Linnéstr. 3, 04103 Leipzig, Germany. E-mail: magdalena.jablonska@uni-leipzig.de*
[b] *Faculty of Chemistry, Jagiellonian University in Krakow, Gronostajowa 2, 30-387 Krakow, Poland*
[c] *Felix Bloch Institute for Solid State Physics, Universität Leipzig, Linnéstr. 5, 04103 Leipzig, Germany*
[d] *Wilhelm-Ostwald-Institute for Physical and Theoretical Chemistry, Universität Leipzig, Linnéstr. 2, D-04103 Leipzig, Germany*
† Electronic supplementary information (ESI) available. See DOI: **https://doi.org/10.1039/d2cy01548j**

solution of either NaOH, TPAOH (tetrapropylammonium hydroxide), HCl, or Na_2H_2EDTA (ethylenediaminetetraacetic acid). Although a broad spectrum of solutions was applied, the catalytic data were provided only for the micro-/mesoporous (5 wt%) Cu/SAPO-34 (with the support treated with an aqueous solution of 0.2 M Na_2H_2EDTA). From these data, it can be observed that NO_x conversion significantly decreased above 300 °C in comparison to conventional Cu/SAPO-34. The authors observed the dissolution and formation of new phases for commercial SAPO-34 treated with an aqueous solution of 0.2 M Na_2H_2EDTA. In line with this, Verboekend *et al.*[17] reported that SAPOs (including SAPO-34) amorphize strongly in an aqueous solution of HCl, H_4EDTA, Na_2H_2EDTA and NaOH (requiring the use of TPAOH or DEA (diethylamine) to preserve their crystallinity during treatment). Furthermore, they pointed out the advantages of zeolites post-modified with DEA (*e.g.*, the zeolites remain in the H-form after removal of DEA, which saves another ion-exchange and the volatility of DEA enables the recovery of 80% of the organic molecules applied[18–20]). Treatment in aqueous solution of DEA is frequently reported to provide zeolites with well-preserved crystallinity and microporosity with larger mesopore sizes (*e.g.*, for beta zeolites).[21] Treatment with aqueous Na_2H_2EDTA is commonly used to remove extra-framework Al from steamed USY zeolites.[22]

In the present study, SAPO-34 was exposed to a post-synthetic treatment in aqueous solutions of DEA and Na_2H_2EDTA. The treatment of SAPO-34 with an aqueous solution of DEA is expected to leach selectively Si from its structure, while the introduced macroporosity is anticipated to allow for enhanced adsorption of copper species on the surface of porous SAPO-34. Otherwise, the treatment with an aqueous solution of Na_2H_2EDTA is expected to leach selectively Al from the external surface, thus, not affecting the internal part of the SAPO-34 crystal. The Cu-containing SAPO-34 catalysts were characterized concerning the structure and morphology (XRD, SEM, TEM, ICP-OES, NMR), texture (low temperature N_2 sorption), acidic properties (FT-IR studies of ammonia sorption), and nature of the copper species (TEM, DR UV-vis, XPS, EPR, FT-IR studies of NO sorption) and were investigated as catalysts for NH_3-SCR-DeNO_x (including rapid scan FT-IR approach). Although Cu-containing SAPO-34 catalysts are frequently investigated for their low- or high-temperature stability,[11] we did not focus our studies on this topic. Otherwise, respective time-on-stream catalytic results are provided.

2. Experimental

2.1 Preparation of micro-/meso-/macroporous Cu-SAPO-34

SAPO-34, used in this study, was prepared by Süd-Chemie GmbH (Bitterfeld, Germany, since 2011 Clariant) following the procedure described by Lok *et al.*[23] Before use, the materials were calcined (550 °C, 4 h, 1 °C min^{-1}). To create mesopores in SAPO-34, it was treated with an aqueous solution of 0.2 M DEA or Na_2H_2EDTA at 65 °C for 2 h under reflux (3 g of zeolite per 100 ml of solution), according to the procedure given by Verboekend *et al.*[17] After treatment, the suspension was cooled down in an ice bath, filtered and washed with water until neutral pH. The obtained materials were again calcined (550 °C, 4 h, 1 °C min^{-1}). In the next step, all the obtained materials were transformed into the NH_4^+-form by triple ion-exchange with 0.5 M NH_4NO_3 performed at 80 °C for 1 h (1 g of zeolite per 100 ml of solution). The resulting sample was again filtrated, washed and dried at room temperature. The NH_4^+-form of SAPO-34 has been reported to improve the mobility of Cu ions and promote the ion-exchange rates and levels.[24] The micro-/mesoporous NH_4^+-SAPO-34 was then ion-exchanged with an aqueous solution of copper(II) acetate (0.05 M) for 24 h at room temperature (1 g of zeolite per 100 ml of solution). Finally, the resulting Cu-containing sample was again filtered, washed, dried at room temperature and calcined (550 °C, 4 h, 1 °C min^{-1}).

2.2 Catalyst physico-chemical characterization

The X-ray powder patterns (XRD) were recorded using a HUBER G670 (Rimsting, Germany) diffractometer applying Cu-K_α radiation (wavelength: 0.154 nm). The samples were measured with a scanning range of the diffraction angle 2θ between 5 and 50° in intervals of 0.005°.

Analysis of Al, Si, Na, and Cu content in the samples was carried out by inductively coupled plasma optical emission spectroscopy (ICP-OES) on a Perkin Elmer, Optima 8000 instrument (Rodgau, Germany). The samples (*ca.* 100 mg) were dissolved in a mixture of hydrofluoric acid (2 cm^3, 48 wt%, Sigma-Aldrich), nitric acid (2 cm^3, 69 wt%, Sigma-Aldrich), and hydrochloric acid (3 cm^3, 35 wt%, Sigma-Aldrich) with microwave radiation (1 h, 200 °C). Before measurement, HF was removed by microwave radiation (5 min, 200 °C) by complexing with H_3BO_3 (12 cm^3, 99.99 wt%, Sigma-Aldrich).

Solid-state nuclear magnetic resonance (NMR) spectra were recorded on a Bruker Avance 750 spectrometer (magnetic field 17.6 T, Rheinstetten, Germany) at a frequency of 195.06 MHz for ^{27}Al. The ^{27}Al experiments were recorded at a spinning frequency of 12 kHz and a recycle delay of 0.1 s. A 1 μs pulse was used that corresponds to about a 30° pulse angle. Spectra are referenced to a 1 M $Al(NO_3)_3$ solution and TMS for ^{27}Al and ^{29}Si, respectively. ^{31}P NMR spectra were recorded on a Bruker Avance 400 spectrometer (magnetic field strength 9.4 T) at a frequency of 161.99 MHz. Direct excitation with a 90° pulse with a length 3 μs and a recycle delay of 6 s was used. Spectra are referenced to concentrated H_3PO_4. Analysis of NMR spectra is done with the dmfit program.[25] In all cases, Gaussian lines have been used for deconvoluting NMR spectra.

The scanning electron microscopy (SEM) images of the samples were obtained with a LEO Gemini 1530 SEM from Zeiss (Oberkochen, Germany) using an accelerating voltage of 10 kV.

Transmission electron microscopy (TEM) measurements were carried out using a JEM-2100Plus instrument from Jeol (Tokyo, Japan) operated at an accelerating voltage of 200 kV. The images were recorded with a 4 K CMOS camera from TVIPS (Gauting, Germany). Sample preparation for TEM was performed by grinding the sample in a mortar and pestle in ethanol, and the dispersed particles were supported on a carbon film coated Ni-TEM grid.

Hg porosimetry analysis was conducted on a Pascal 140 (Thermo Fisher Scientific, Waltham, Massachusetts, USA) for data points from pressures up to 250 kPa and a Pascal 440 (Thermo Fisher Scientific, Waltham, Massachusetts, USA) for data points from pressures between 250 kPa and 400 MPa. Prior to the analysis, samples were evacuated at 0.02 kPa for 10 min at room temperature. The contact angle used was 140° with a surface tension of 0.48 N m^{-1}. The pore width was calculated by the Washburn equation from the intrusion curve.[26] The meso- and macropore widths correspond to the modal mesopore width and modal macropore width, respectively. For analysis, a fraction of particle size in the range of 200–400 μm was used.

Nitrogen sorption isotherms were obtained at −196 °C using a MicrotracBEL Corp., BELSORP-miniX (Haan/Duesseldorf, Germany). Before measurement, *ca.* 100–200 mg of the sample was activated at 250 °C and 1 Pa. The total pore volume was taken from the point $p\ p_0^{-1}$ = 0.9875. The specific surface area was calculated using the Brunauer–Emmett–Teller (BET) method and the pore width distribution was obtained using the Barrett–Joyner–Halenda (BJH) method. The micropore volume and specific surface area of micropores were calculated using the Harkins and Jura model (*t*-plot analysis, thickness range of 0.95–1.12 nm).

The catalysts were subjected also to *in situ* diffuse reflectance UV-vis (DR UV-vis) studies to follow the susceptibility of the catalysts to a water vapour-rich atmosphere. The samples in the form of self-supported discs were placed in a Praying Mantis® coupled with a UV-vis spectrometer (Shimadzu UV-2600, Berlin, Germany) and then were heated at a rate of 5 °C min^{-1} to 400 °C in a flow of synthetic air (30 ml min^{-1}) and the temperature was maintained for 0.5 h, then cooled down to room temperature and stepwise heated to 400 °C (at a rate of 5 °C min^{-1}) in the flow of synthetic air saturated with H_2O.

The X-ray photoelectron spectroscopy (XPS) experiments were performed using a Focus CSA-150 electron energy analyser (Hünstetten-Kesselbach, Germany). Excitation was supplied by unmonochromatized Al and Mg K_α. Spectra have been recorded with a pass energy of 100 eV resulting in an overall resolution of about 2 eV. The samples have been pressed as pellets and mounted with Tantalum stripes. Heating steps have been reached by using a filament heater. Data analysis has been performed using UNIFIT software.[27]

The electron paramagnetic resonance (EPR) measurements of the samples were carried out with a Bruker EMX micro (X-band, 9.4 GHz, Rheinstetten, Germany) spectrometer equipped with an Oxford Instruments He cryostat ESR 900. The spectrometer was fitted with an ER 4119 HS resonator. The EPR spectral simulations were performed using the MATLAB simulation package EasySpin.[28] The microwave power was adjusted such that no line shape distortion occurred, whereas the modulation amplitude was set to 1 mT to improve the sensitivity. Powder samples (~10 mg) were put into an EPR quartz glass with a 3.8 mm inner diameter and then sealed to avoid contact with air. The activation procedure was carried out on each sample at 200 °C for 2 h under vacuum conditions to dehydrate the samples for comparison with calcined (550 °C for 4 h in static air) samples.

Before Fourier transform infrared spectroscopy (FT-IR) studies, the catalysts were formed into the form of self-sustaining pellets (*ca.* 5–10 mg cm^{-2}) and pretreated *in situ* in a custom made quartz IR cell at 500 °C under vacuum conditions for 15 min followed by pure oxygen treatment at the same temperature for 1 h. After evacuation and cooling down to room temperature, the spectrum was taken. The concentration of both Brønsted and Lewis acid sites was determined in quantitative *in situ* IR studies with NH_3 (PRAXAIR, ≥99.8 vol%) as a probe molecule. An excess of ammonia, sufficient to neutralise all acid sites, was adsorbed at 130 °C, followed by an evacuation at the same temperature. The FT-IR spectrum free of the gaseous and physisorbed ammonia molecules was taken at a temperature of 130 °C. The concentration of Brønsted and Lewis sites was calculated using respectively the intensities of the 1455 cm^{-1} band of ammonium ions (NH_4^+) and the 1621–1611 cm^{-1} band of ammonia coordinatively bonded to Lewis sites (NH_3L) by applying the respective absorption coefficients, *i.e.*, 0.11 and 0.026 $cm^2\ mol^{-1}$ for the NH_4^+ and NH_3L band, respectively.[29,30] Before adsorption, nitric oxide (Linde Gas, 99.5 vol%) was purified by the freeze–pump–thaw technique. The adsorption of nitric oxide upon saturation of copper sites followed by oxygen adsorption (MERCK, 99.5 vol%) was performed at room temperature. Then the temperature was raised to 150 °C when NH_3 was introduced. The spectra were recorded with a Bruker Vertex 70 spectrometer (Ettlingen, Germany) in standard scanning mode (one spectrum was accumulated within 30 s) equipped with a mercury cadmium telluride (MCT) detector with a spectral resolution of 2 cm^{-1}. All of the spectra presented in this work were normalized to 10 mg of a sample.

For rapid scan FT-IR studies of NH_3-SCR-DeNO_x, the portion of reagent mixture containing 4NO (1000 μmol) + O_2 (1000 μmol) + $4NH_3$ (1200 μmol) + H_2O (1000 μmol) was brought into contact with the catalyst at 150 °C. The reaction progress was tracked for 300 s by accumulating spectra within 0.3 s each, while other measurement parameters have not changed.

2.3 Catalytic experiments

The catalytic experiments were carried out in a fixed-bed quartz tube reactor (inner diameter: 6 mm, length: 200 mm).

For catalytic experiments, a fraction of particle size in the range of 200–400 μm was used. Before each experiment, the catalysts (m_K = 0.2 g) were activated at 350 °C for 1.5 h under a flow of 50 ml min^{-1} of He and then cooled down to 50 °C. After that, the simulated flue gas, with a total flow rate (F_{TOT}) of 120 ml min^{-1} composed of 500 ppm NO, 575 ppm NH_3 and 4 vol% O_2 and balance He, was switched on to pass through the catalyst bed. For selected samples, the catalytic tests were carried out in the presence of water vapor (5.0 vol%). The gas hourly space velocity (GHSV) was determined to be ~30 000 h^{-1}. The reaction was carried out at atmospheric pressure and in a range of temperatures from 50 °C to 450 °C with an interval of 25–50 °C. At each temperature, the reaction was stabilized for 70 min before the quantitative analysis of NO and N_2O concentration. The gas leaving the reactor is washed in a gas-washing bottle filled with concentrated phosphoric acid. The NO_x-converter was used to reduce NO_2 to NO, to measure the total concentration of NO_x. Analysis of NO and N_2O was performed using a non-dispersive infrared sensor (NDIR) URAS 10E Fa. Hartmann und Braun (Frankfurt a. M., Germany). The conversion of NO (X(NO)) was determined according to $X(NO) = ([c(NO)_{in} - c(NO)_{out}]/c(NO)_{in}) \times 100\%$, where $c(NO)_{in}$ and $c(NO)_{out}$ – concentration of NO in the inlet and the outlet gas, respectively. The yield of N_2O ($Y(N_2O)$) was calculated based on the following equation: $Y(N_2O) = (2 \times c(N_2O)/[c(NO)_{in} + c(NH_3)_{in}]) \times 100\%$, where $c(N_2O)$, $c(NO)_{in}$, and $c(NH_3)_{in}$ – concentration of N_2O in the outlet gas and the concentration of NO and NH_3 in the inlet gas, respectively. The experimental uncertainty of the calculated conversion was found to be ±2% as indicated by repeated measurements of identical catalysts.

3. Results and discussion

3.1 Structure and texture of the materials

Fig. 1 shows the XRD patterns of the calcined SAPO-34 and prepared Cu-containing SAPO-34. All the samples exhibit typical diffraction reflections of the chabazite (CHA) structure, but the intensity varied among the samples. The structure of SAPO-34 is preserved after the post-modification with an aqueous solution of Na_2H_2EDTA or DEA and, as expected, a lowered crystallinity of Cu-containing SAPO-34 was evidenced. The crystallinity of both materials decreased to 36–45% in comparison to Cu-SAPO-34 (100%). No additional phases were observed in the XRD patterns after DEA and Na_2H_2EDTA treatment, in contrast to earlier studies[16] evidencing dissolution and formation of new phases for commercial SAPO-34 (Clariant, 3.5 wt% Si, 20.2 wt% Al, 55.8 wt% O, 18.7 wt% P, and 1.8 wt% Ti) treated with an aqueous solution of 0.2 M Na_2H_2EDTA. Furthermore, Verboekend *et al.*[17] applied also commercial SAPO-34 (ACS Material, 6.5 wt% Si, 20.0 wt% Al, 52.6 wt% O, 20.9 wt% P). They reported that for SAPO-34 treated in a 0.4 M aqueous solution of DEA, a weight loss of 15% was observed, while completely preserving the structure. The preservation of the SAPO-34 structure was ascribed to a relatively small kinetic diameter of DEA, enabling it to enter the micropore cavities. In our case, the crystallinity of SAPO-34 was lost during the treatment in an aqueous solution of 0.4 M DEA (results not shown). Otherwise, the structure of SAPO-34 was preserved after post-synthetic treatment in an aqueous solution of 0.4 M Na_2H_2EDTA. Furthermore, there are no obvious diffraction peaks, including CuO_x (2θ = 35.6, 36.4 and 38.8°) or $CuAl_2O_4$ (2θ = 37.1°) species observed in the XRD pattern, leading to the conclusion that the introduced copper species are highly dispersed on the catalyst surface. Table 1 represents the results obtained from the ICP-OES analysis. Furthermore, the respective n(Si)/n(Al) and n(Cu)/n(Al) were calculated. The modification of the porosity of SAPO-34 affects the content of the introduced copper species. Thus, for the Cu-SAPO-34_Na_2H_2EDTA and Cu-SAPO-34_DEA samples, the copper content varied from 1.0 to 2.6 wt%, respectively, compared to Cu-SAPO-34 (containing only 0.5 wt%). A similar effect was reported before for the post-modified ZSM-5 (ref. 31 and 32) and Y (ref. 33) zeolites, however, it was not yet explained.

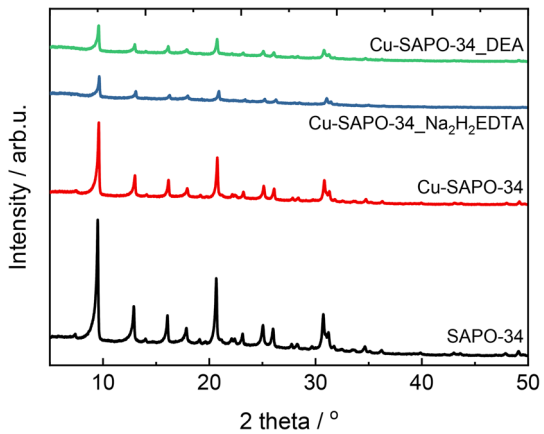

Fig. 1 XRD patterns of commercial SAPO-34 and Cu-containing SAPO-34; sample labels as in Table 1.

Fig. 2 shows the SEM images of Cu-containing SAPO-34. There are no changes in the crystal size and shape, thus no hints of degradation after ion-exchange with copper species were observed for all the copper-containing samples. The Cu-SAPO-34 sample possesses a cubic morphology of the crystals with a smooth crystal surface and broader size distribution of 1–5 μm. In contrast, SEM images of both dealuminated Cu-SAPO-34_Na_2H_2EDTA and desilicated Cu-SAPO-34_DEA allow for the identification of macropores which in the latter material were effectively distributed in the internal part of crystals, producing a sponge-like material. Still, the size and shape of the crystals remain unaffected. Indeed, the representative TEM images (Fig. 3) of the sample Cu-SAPO-34_DEA reveal the intracrystalline macropores with different sizes on its surface, whereas the other samples do not show this type of porosity. These findings indicate that the Na_2H_2EDTA dealumination effect is superficial in nature, as opposed to DEA. By employing high angle annular dark-field (HAADF) scanning transmission electron microscopy (STEM),

Table 1 The results of the elemental analysis of SAPO-34 and Cu-containing SAPO-34; (ω_i: mass fractions)

Sample	ω_{Al}/wt%	ω_{Si}/wt%	ω_P/wt%	ω_{Cu}/wt%	n(Si)/n(Al)	n(Cu)/n(Al)
SAPO-34	17.5	3.2	14.9	—	0.18	—
SAPO-34_Na_2H_2EDTA	17.7	4.6	15.8	—	0.25	—
SAPO-34_DEA	18.9	5.1	14.3	—	0.26	—
Cu-SAPO-34	16.7	3.7	15.9	0.5	0.21	0.01
Cu-SAPO-34_Na_2H_2EDTA	18.5	3.8	16.6	1.0	0.20	0.02
Cu-SAPO-34_DEA	19.1	4.5	15.3	2.6	0.23	0.06

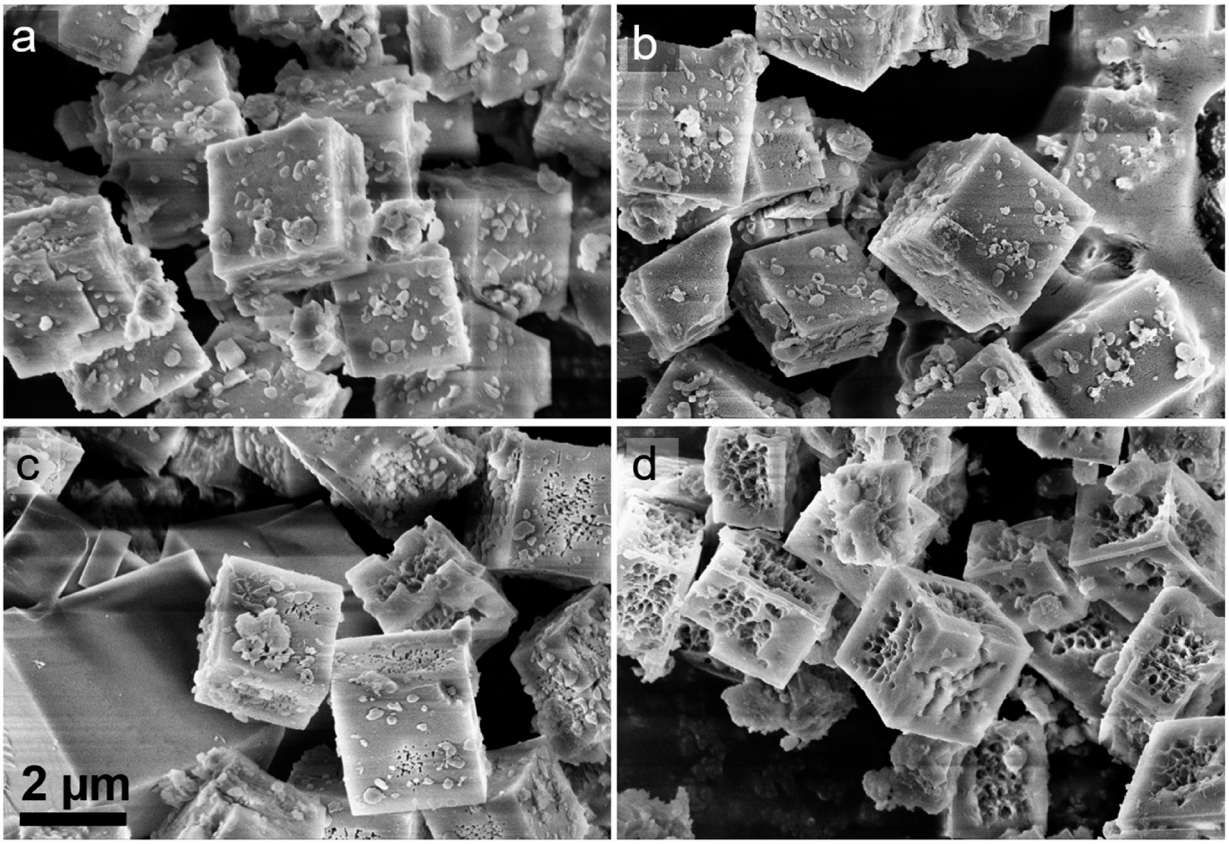

Fig. 2 SEM images of a) SAPO-34, b) Cu-SAPO-34, c) Cu-SAPO-34_Na_2H_2EDTA, and d) Cu-SAPO-34_DEA.

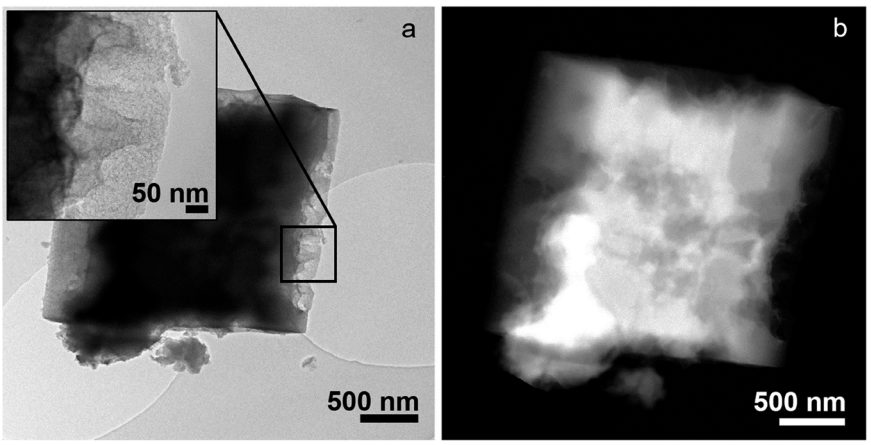

Fig. 3 a) TEM overview and high-resolution image (inset) and b) corresponding HAADF-STEM material contrast image of Cu-SAPO-34_DEA.

no material inhomogeneities were found, except for the additional pores at the crystal surfaces of the Cu-SAPO-34_DEA sample (Fig. 3b). The existence of a macropore structure is further confirmed by the porosity measurement *via* mercury intrusion (Fig. SI1†). A monomodal pore width distribution with a median pore width of 568 and 693 nm for Cu-SAPO-34_Na_2H_2EDTA and Cu-SAPO-34_DEA, respectively, is verified. The intruded mercury at 100 μm appears due to the filling of interparticle voids. The developed macroporosity allows for more efficient adsorption of copper species on the surface of defects and leads to a higher n(Cu)/n(Al) ratio of 0.02 and 0.06 for Cu-SAPO-34_Na_2H_2EDTA and Cu-SAPO-34_DEA, respectively, than that of Cu-SAPO-34 (0.01).

Fig. 4 presents the ^{27}Al and ^{31}P MAS NMR spectra of SAPO-34 and Cu-containing SAPO-34. The ^{27}Al NMR spectra contain four-, five- and six-coordinated aluminum signals at *ca.* 44, 17, and −9 ppm, respectively. About half of the intensity is assigned to four-coordinated aluminum. The amount of five-coordinated aluminum increases from 5 to 14% from SAPO-34 to the post-synthetically modified SAPO-34 with Na_2H_2EDTA or DEA on the cost of six-coordinated aluminum in the Cu-containing samples (Table SI1†). An increase in five-coordinated aluminum intensity was also observed in a related system together with a stronger increase in six-coordinated aluminum, explained by the formation of one or two Al–OH linkages leading to five- and six-coordinated aluminum sites.[12,29,34] The significant amount of six-coordinated aluminum present already in the starting SAPO-34 material makes this material more susceptible to post-synthetic treatment with Na_2H_2EDTA or DEA. Hydrolysis of Al–O and Si–O bonds leads to the increase of the amount of defect sites, *i.e.*, five- and six-coordinated aluminum species. Compared to the conventional SAPO-34, Cu-SAPO-34 and its porous analogues show more tetra- and penta-coordinated and fewer octahedral aluminum atoms. It evidences that both Na_2H_2EDTA and DEA, and the ion-exchange procedure led to cleaning the micropores of SAPO-34 from extraframework Al^{VI} species. Thanks to that, the accessibility of reagents within CHA cages is less restricted.

All the samples exhibit a narrow peak at *ca.* −26 ppm and a broader one at *ca.* −20 ppm in the ^{31}P spectra (Fig. 4b), with a roughly 2 : 1 intensity ratio (Table SI2†). The signal at −20 ppm corresponds to P atoms coordinated with water molecules in the form of species P(OAl)$_x$(H$_2$O)$_y$.[35–37] This peak gets slightly more intense in the Cu-containing post-synthetically modified materials, indicating a higher possibility of P species' hydration due to the accommodation of higher amounts of water in porous materials (Cu-SAPO-34_Na_2H_2EDTA and Cu-SAPO-34_DEA). All the signals resemble tetrahedral phosphorous P(4Al). In principle, there is a relation between the ^{31}P shift and the P–O–Al angle,[38] indicating P–O–Al angles of 145° and 140° for the peaks at −26 and −20 ppm, respectively. A general agreement of the observed shifts with published data exists.[39] An influence of paramagnetic copper can be ruled out as linewidths are comparable also for SAPO-34 containing no copper species.

Fig. 5 presents the N_2 sorption isotherms and derived pore width distribution of Cu-containing SAPO-34. The microporous SAPO-34, Cu-SAPO-34 and Cu-SAPO-34_Na_2H_2-EDTA show the type-I N_2 adsorption–desorption isotherm, while Cu-SAPO-34_DEA exhibits a type-IV isotherm with a hysteresis loop in the region $0.80 < P\,P_0^{-1} < 1.0$ due to capillary condensation in the meso- and macropores. In particular, Cu-SAPO-34_DEA exhibits an increased mesopore volume of 0.05 cm^3 g^{-1} compared to 0.01 cm^3 g^{-1} of microporous materials (Table 2). Furthermore, the pore width distribution clearly shows the presence of mesopore structure with pore sizes centred at 4.7–16 nm, while the pore width distribution is relatively concentrated. Together with the abovementioned SEM and TEM analyses, the nitrogen adsorption results strongly demonstrate the existence of meso- and macropores in Cu-SAPO-34_DEA. The specific surface area of the samples with a post-modified support (*i.e.*, Cu-SAPO-34_Na_2H_2EDTA and Cu-SAPO-34_DEA) is lower compared to that of Cu-SAPO-34. The lower A_S(BET) values for micro-/mesoporous Cu-containing SAPO-34 compared to the conventional material agree with other studies (*e.g.*, ref. 12). Otherwise, Li *et al.*[15] and Mi *et al.*[13] claimed that the generation of mesopores increases the specific surface area.

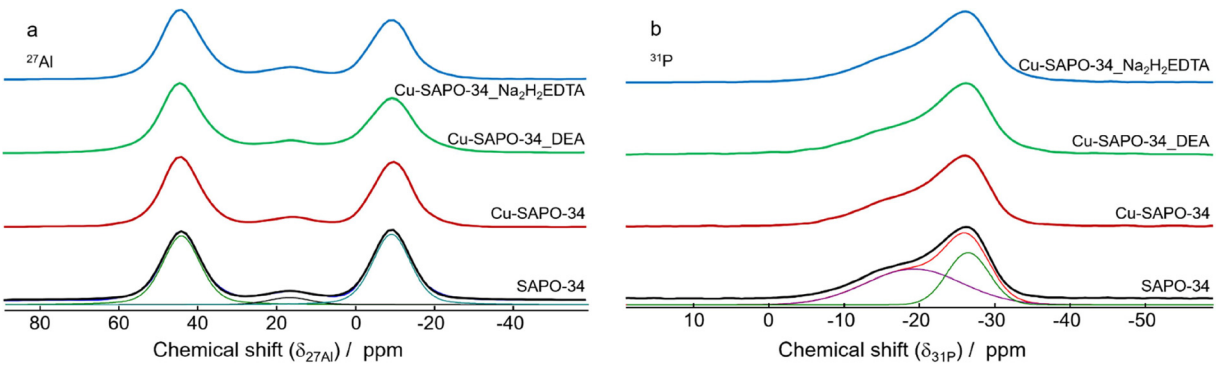

Fig. 4 a) ^{27}Al MAS NMR and b) ^{31}P MAS NMR spectra of Cu-containing SAPO-34. The deconvolution is given for the lowest spectrum only for clarity.

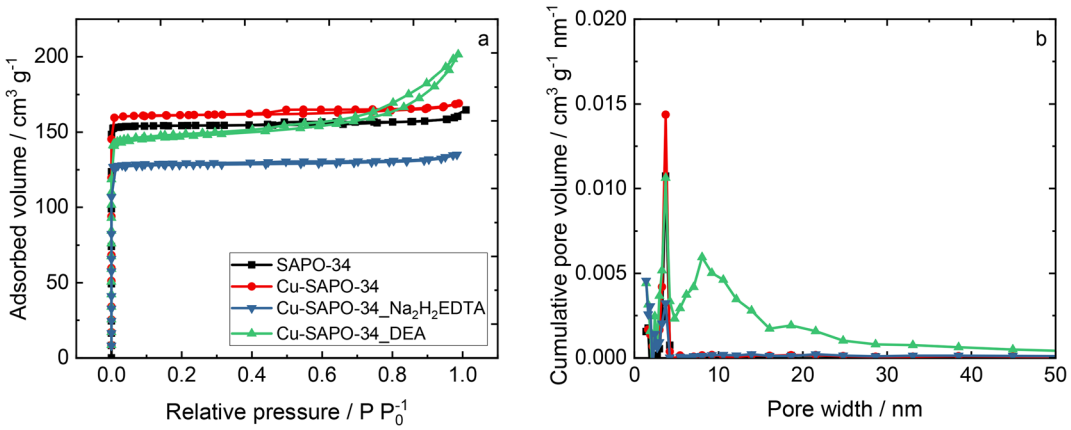

Fig. 5 a) N_2 sorption isotherms and b) pore width distribution of Cu-containing SAPO-34.

Table 2 Textural properties of the samples determined from the N_2 sorption measurements: specific surface area (A_S(BET)), micropore pore volume (V_{MIC}), mesopore pore volume (V_{MES}) and total pore volume (V_{TOT}), acidic properties of the samples determined from ammonia adsorption: concentration of Brønsted and Lewis sites, respectively ($C_{Brønsted}$, C_{Lewis})

Sample	A_S(BET)/m^2 g^{-1}	$V_{(TOT)}$/cm^3 g^{-1}	$V_{(MIC)}$/cm^3 g^{-1}	$V_{(MES)}$/cm^3 g^{-1}	$C_{Brønsted}$/μmol g^{-1}	C_{Lewis}/μmol g^{-1}
SAPO-34	468	0.25	0.24	0.01		
Cu-SAPO-34	491	0.26	0.25	0.01	289	65
Cu-SAPO-34_Na_2H_2EDTA	401	0.21	0.20	0.01	270	115
Cu-SAPO-34_DEA	458	0.31	0.26	0.05	181	125

3.2 Acid-redox properties of the materials

Information on the acidic properties of redox catalysis is crucial for defining their adsorption feature and thus reaction path. The analysis of the position and intensities of the OH groups in IR data informs, at the first glance, about the extent of the NH_4^+/Cu^{2+} ion-exchange procedure and the possible formation of Cu^{2+}(OH) moieties. Different types of copper species on Cu-containing SAPO-34, including isolated Cu^{2+} ions, Cu^{2+}(OH), $[Cu–O–Cu]^{2+}$ and small CuO_x nanoclusters (typically found on the exterior surface of the molecular sieve crystals) were approved *via* combining IR spectroscopy of probe molecule sorption, *e.g.*, NH_3, CO, NO adsorption *etc.*, and theoretical calculations.[40] Fig. 6 presents the IR spectra of the Cu-containing SAPO-34 catalysts collected in the O–H stretching vibration region, and upon ammonia adsorption in the N–H deformation vibration region. All the materials possess two kinds of acidic Si(OH)Al groups identified by the bands at 3625 and 3595 cm^{-1} and located in eight- and six-membered rings (MRs), respectively. The proportion between Si(OH)Al_{8MR} and Si(OH)Al_{6MR} is kept for all the catalysts, indicating the lack of any preference in Cu^{2+} location in 8MR and 6MR channels in the materials

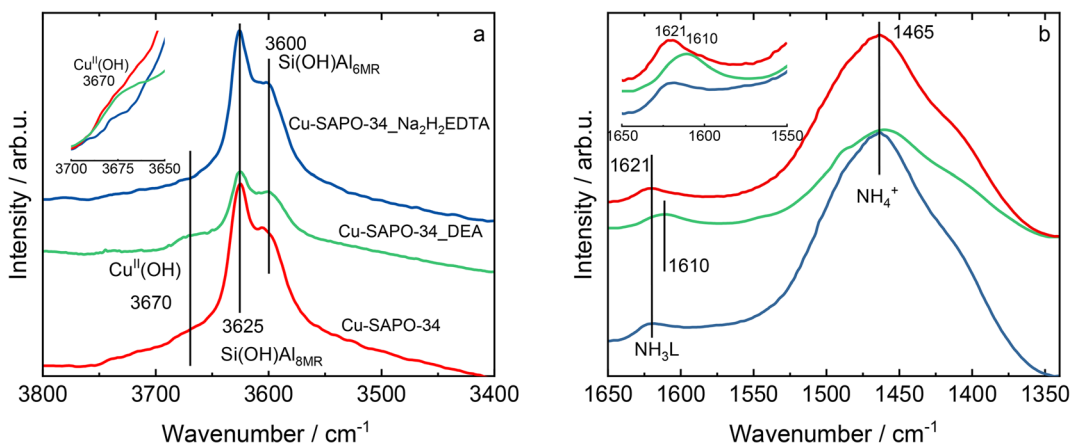

Fig. 6 The IR spectra of Cu-containing SAPO-34 collected in a) the O–H stretching vibration region (the Cu^{2+}–OH bands zoomed in the inset), and b) upon ammonia adsorption in the N–H deformation vibration region (NH_3L bands zoomed in the inset); a) and b) samples labels are equal.

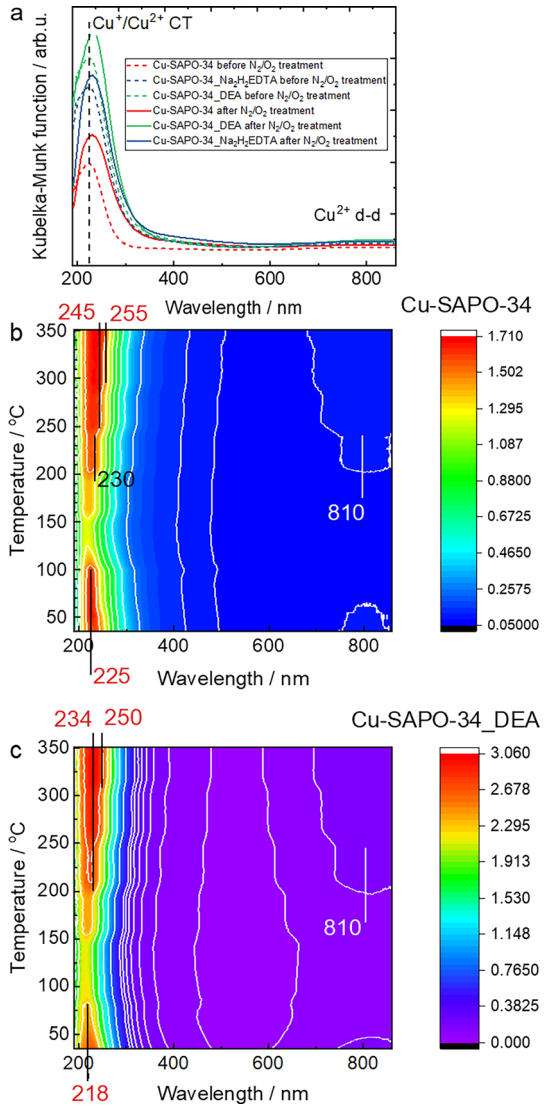

Fig. 7 a) DR UV-vis spectra collected at room temperature (*ca.* 25 °C) of Cu-SAPO-34 and Cu-SAPO-34_DEA upon the dehydration step (400 °C, 0.5 h, synthetic air) followed by oxidation under synthetic air (N_2/O_2) conditions, and *operando* DR UV-vis spectra (given as the maps) presenting the changes in copper site speciation in b) Cu-SAPO-34, and c) Cu-SAPO-34_DEA during the water vapor and synthetic air treatment at increasing temperatures.

studied. The substitution of Cu^{2+} for NH_4^+ in ion-exchange positions is more distinct in Cu-SAPO-34_DEA (the decrease by 50% of the Si(OH)Al band intensities) than in Cu-SAPO-34. This is in line with the highest n(Cu)/n(Al) value and the highest intensity of the oxygen to Cu^{2+} charge transfer of the DR UV-vis band (Fig. 7). The band at 3670 cm^{-1} originates from OH species attached to Cu^{2+} cations, again the most populated in Cu-SAPO-34_DEA (Fig. 6a, inset).

All the copper(II) species, *i.e.*, Cu^{2+}, Cu^{2+}(OH) and $[Cu–O–Cu]^{2+}$, are the sources of Lewis acidity, which together with Brønsted sites were determined in quantitative IR studies of ammonia sorption. The use of an ammonia probe meets the expectation of the employment of reagent molecules to examine the acidic properties of solid catalysts. In contrast to temperature-programmed NH_3 desorption studies, the IR approach allows for calculating the concentration of the Brønsted and Lewis sites independently from each other. Upon the saturation of all acidic sites with ammonia, the low frequency region is dominated by two maxima at *ca.* 1620 and 1465 cm^{-1} (Fig. 6b). These two maxima are assigned to the asymmetric bending N–H vibration of molecular NH_3 adsorbed on Cu^{2+} Lewis sites and to the bending N–H vibration of NH_4^+ ions stabilized on $Si(O^-)Al$ sites, respectively.[41] According to data collected in Table 2, both Cu-SAPO-34 and Cu-SAPO-34_Na_2H_2EDTA accommodate a similar number of Brønsted acid sites, while in Cu-SAPO-34_DEA the number of protonic sites detected with ammonia is *ca.* 65% of the values found for the abovementioned materials. The substitution of NH_4^+ for Cu^{2+} species was deduced previously from the lowest intensities of Si(OH)Al groups in Cu-SAPO-34_DEA. The number of Lewis sites (NH_3L) increases with n(Cu)/n(Al) (Table 1). Thus, Cu-SAPO-34_DEA accommodates a two-fold higher number of Lewis sites than Cu-SAPO-34. Special attention should be paid to the NH_3L band position in the Cu-SAPO-34_DEA material. It is (1610 cm^{-1}) significantly lower than in other materials (1621 cm^{-1}) documenting vital differences in the strength of Lewis sites resulting from ammonia ligation also to Cu^{2+}(OH) and $[Cu–O–Cu]^{2+}$ sites. Both the type of anion ligated (OH^- *vs.* O^{2-}) and neighboring vicinity of the zeolite framework influence the electron-acceptor properties of the exchangeable cationic sites, thus the unambiguous assignment of the NH_3–L band to the respective copper sites is not feasible.

To explore the aggregation state of Cu species in the samples, DR UV-vis spectra measurements were carried out. Fig. 7a shows the DR UV-vis spectra of Cu-containing SAPO-34 (calcined at 550 °C for 4 h in static air). All the catalysts show the band maximum below 250 nm, which is attributed to oxygen-to-metal charge transfer related to Cu^+ or Cu^{2+} cations stabilized by the zeolite framework.[42,43] The bands in the range of 250–600 nm proved the presence of the CuO species and $[Cu–O–Cu]^{2+}$ species.[31,44] The absorption in the range 600–900 nm is related to the d–d transitions of Cu^{2+} ions in pseudo-octahedral coordination (*e.g.*, $Cu(H_2O)_6^{2+}$).[42,43] The shift of the bands indicates a decrease in the dispersion of Cu species. The isolated $Cu^{+/2+}$ ions in Cu-containing SAPO-34 are suggested to be located near the center of 6MRs in the d6r sub-unit of CHA,[45,46] while $[Cu–O–Cu]^{2+}$ species (as the product of dehydrating of $Cu(OH)^+$ at exchange positions) adjoined to eight-membered rings (8MRs).[47,48] The resistance of copper species toward the water-rich atmosphere was further evaluated in *in situ* DR UV-vis studies. In the first stage of the experiments, the calcined materials were pretreated in a synthetic air atmosphere in the temperature range (RT, *ca.* 25 °C) up to 400 °C. Fig. 7a displays the DR UV-vis spectra collected at RT in N_2/O_2-atmosphere (*i.e.*, synthetic air) for Cu-SAPO-34 and Cu-SAPO-34_DEA before and after heating to 400 °C. For both

catalysts, a significant increase in the intensity of the band associated with ligand-to-metal charge transfer (LTMCT) transitions and its shift towards higher wavelengths is noticed (from 210 to 250 nm). The shift to higher wavelengths and the intensity increase observed upon thermal treatment at 400 °C in synthetic air are the result of water ligand removal from the coordination sphere of Cu^{2+}, which forces the latter species to interact with the oxygen atoms of the zeolitic framework. Substitution of water ligands with framework oxygen atoms brings the lowering of local symmetry of Cu^{2+} explaining the observed spectral behavior in analogy with that found for homogeneous complexes.[49] The effect of the lowering of local symmetry of Cu^{2+} upon water ligand removal is even more pronounced for narrow pores and small cage materials due to preferable locating of bare exchangeable Cu^{2+} cations in 6MRs and 8MRs. Oxidation by molecular oxygen is an activation process and does not occur in a water-free environment at room temperature. However, upon contact with synthetic air at 400 °C, the low intensity band at 410 nm appears as the result of the generation of some $[Cu–O–Cu]^{2+}$ species. All the effects discussed above are more pronounced for Cu-SAPO-34_DEA.

The effect of water vapor present in the synthetic air flow is visualized in Fig. 7b and c, which display the *operando* DR UV-vis spectra of pre-oxidized (in synthetic air) Cu-SAPO-34 and Cu-SAPO-34_DEA heated from room temperature (*ca.* 25 °C) up to 400 °C. As stated previously, the LTMCT transitions at 218 nm identify the exchangeable Cu^{2+} cations with water ligands. In the temperature range of 100–160 °C, the 218 nm band intensity is decreased due to the changes in cupric Cu^{2+} ion coordination sphere and higher dispersion of previously aggregated Cu^{2+} species. This high dispersion facilitates the mobility of copper species and their accumulation in the internal part of SAPO-34 grains at increasing temperatures. Further, at temperature as high as 200 °C, the new bands at 234 nm and 810 nm start to again develop and at 300 °C another band appears at 250 nm. Therefore, it can be concluded that the additional number of Cu^{2+} exchangeable cations appears in the presence of both oxygen and water vapor but also the conditions for Cu^{+} reoxidation by molecular oxygen are changed in the presence of H_2O. From the spectra displayed in Fig. 7, it can be concluded that reoxidation of Cu^{+} by molecular oxygen does not take place under dry synthetic air conditions (Fig. 7a) but occurs easily when water vapor is admitted to synthetic air (Fig. 7b and c). The rehydration facilitates noticeably an efficient oxidative effect of molecular oxygen at temperature as high as 160 °C directly leading to Cu^{2+}–OH moieties (250 nm) and the same type of copper species present in the calcined material (810 nm). The reoxidation of Cu^{+} to Cu^{2+} has been confirmed by XANES and vis-near-IR spectroscopy.[49–53] Again, copper sites in Cu-SAPO-34_DEA appear to be the most susceptible to oxidation in water vapor.

To gain insight into the surface composition and the nature of active species, XPS was employed to identify the valence state of copper species on the surface of the catalyst.

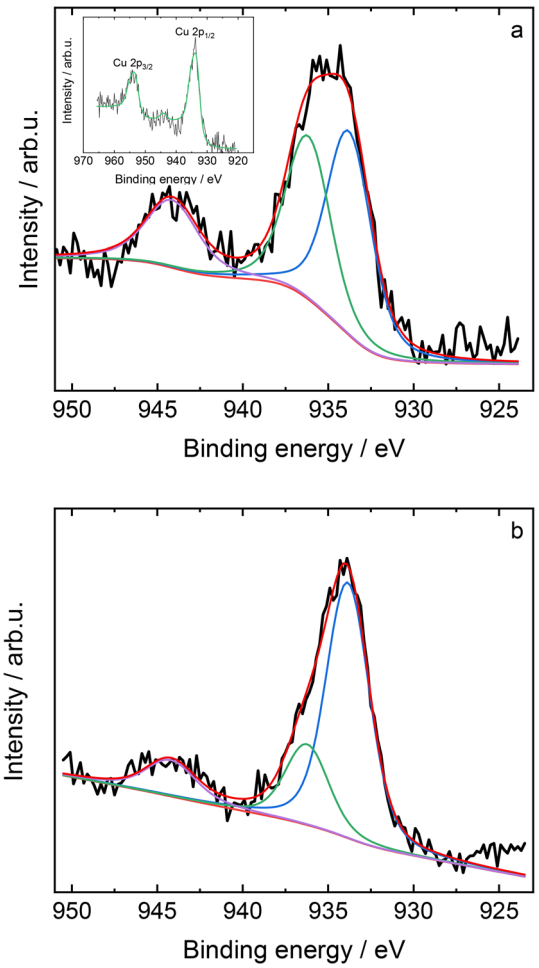

Fig. 8 Representative Cu $2p_{3/2}$ spectra of Cu-SAPO-34_DEA with the fitted components for a) room temperature (*ca.* 25 °C) and b) after heating to 250 °C under vacuum. The inset in a) shows the complete Cu 2p spectrum.

Given the surface sensitive nature, and the fact that materials are treated under high vacuum conditions which leads to autoreduction of Cu^{2+} to Cu^{+} at elevated temperatures, the XPS results have to be handled with care. The general structure of the Cu 2p spectra shown as the inset in Fig. 8a is given by the Cu $2p_{3/2}$ and Cu $2p_{1/2}$ peaks located at around 935 and 954 eV. These peaks with shake-up satellite peaks located at binding energies approximately 10 eV higher than the respective main peaks are essentially characteristic of Cu^{2+} species.[54,55] Cu^{+} contributions are expected at lower binding energies (about 932.4 to 933.2 eV for Cu $2p_{3/2}$).[55–57] In the current analysis, they are not separately fitted in order to keep the number of parameters low, but they might contribute to the low binding energy part. The Cu 2p XPS spectra of conventional Cu-SAPO-34 (0.5 wt% of Cu, see Fig. SI2a†) can be described by only one main peak located at a binding energy of around 934.1 eV and originating solely from isolated Cu^{2+} cations balancing the negative charge of the SAPO-34 framework. Such an assumption is justified by the lowest Cu loading for this material among the samples

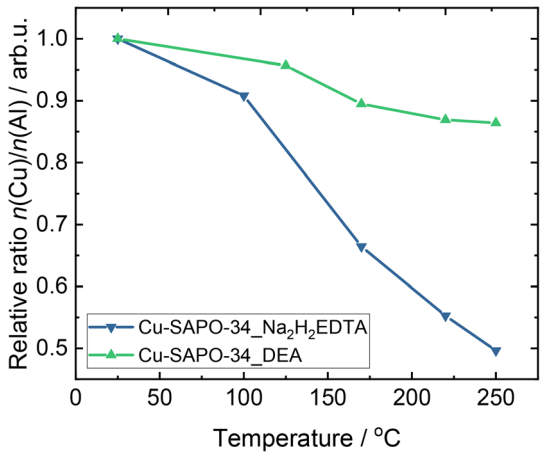

Fig. 9 Temperature-dependent decrease of the n(Cu)/n(Al) ratio for Cu-SAPO-34_Na_2H_2EDTA and Cu-SAPO-34_DEA derived from XPS data.

studied. As can be seen from the signal-to-noise ratio, however, this amount of Cu species is at the edge of being properly detected, with the satellite disappearing in the noise level. The data for Cu-SAPO-34_Na_2H_2EDTA (Fig. SI2b†) and Cu-SAPO-34_DEA (Fig. 8a) have been fitted with two different contributions for the main peaks: at around 933.5–933.7 eV the contribution of Cu^{2+} in oxoclusters of various dispersion degrees, while at around 935.3–935.7 eV isolated exchangeable Cu^{2+} species are still present.[57] The apparent absence of Cu^{+} species in the samples was further approved *via* IR sorption with NO (Fig. 10). The satellite peak located at *ca.* 944 eV becomes visible for the materials with higher copper loading, *i.e.*, Cu-SAPO-34_Na_2H_2EDTA and Cu-SAPO-34_DEA (Fig. SI2† and 8a, respectively) where aggregated copper(II) oxospecies are found. Indeed, the DR UV-vis analysis reveals a decrease in the dispersion of Cu species in both post-synthetic modified materials (Fig. 7a).

To evaluate the influence of temperature, a heating series under vacuum from room temperature to 250 °C was also performed (Fig. 8a and b). Upon heating the lower binding energy component (933.5–933.7 eV) significantly increases (at the expense of the higher binding energy component (935.3–935.7 eV) and the satellite), which can be assigned to advanced olation and oxolation processes resulting in the oxospecies formation. The XPS results of copper surface content (n(Cu)/n(Al) = 0.02 and 0.05 for Cu-SAPO-34_Na_2H_2EDTA and Cu-SAPO-34_DEA, respectively) reflected the ICP-OES results reporting the significantly higher ability of the DEA treated material to accommodate copper species. In addition, for both Cu-SAPO-34_DEA and Cu-SAPO-34_Na_2H_2EDTA, a reduction in the n(Cu)/n(Al) ratio was observed with increasing temperature (and time) under vacuum (Fig. 9). While this ratio decreased by 50% for Cu-SAPO-34_Na_2H_2EDTA, the decrease was only by 15% in the case of Cu-SAPO-34_DEA which directly relates to the exclusive loss of some amount of copper species from the XPS detection zone. Such loss indicates for the ability of copper species to migrate from the external surface to the interior zone of the crystal. Despite of the highest content of the oxospecies on the external surface of the DEA-treated material, the high accumulation of isolated Cu^{2+} cations confirmed in IR studies (the highest concentration of Cu(II)-mononitrosyls and the presence of the Cu^{2+}–OH band) still ensures its enhanced NH_3-SCR-DeNO_x activity as will be discussed later on. The presence of Cu^{+} formed as a result of copper(II) autoreduction after long exposure to X-rays under high vacuum cannot be ruled out, and therefore its participation in the lower energy component (933.5–933.7 eV) as well. The presence of water vapor with a pressure of 1×10^{-4} mbar during heating did not change the observations.

Furthermore, EPR spectroscopy is applied to investigate the paramagnetic valency state (Cu^{2+}) of the introduced copper ions. We must note that, whereas isolated Cu^{2+} ions are EPR active, other copper species such as $[Cu–O–Cu]^{2+}$ (antiferromagnetic case) and Cu^{+} (diamagnetic case) are EPR silent.[7,58] The analysis of the Cu^{2+} EPR powder spectra provides the principal values of the g tensor of the

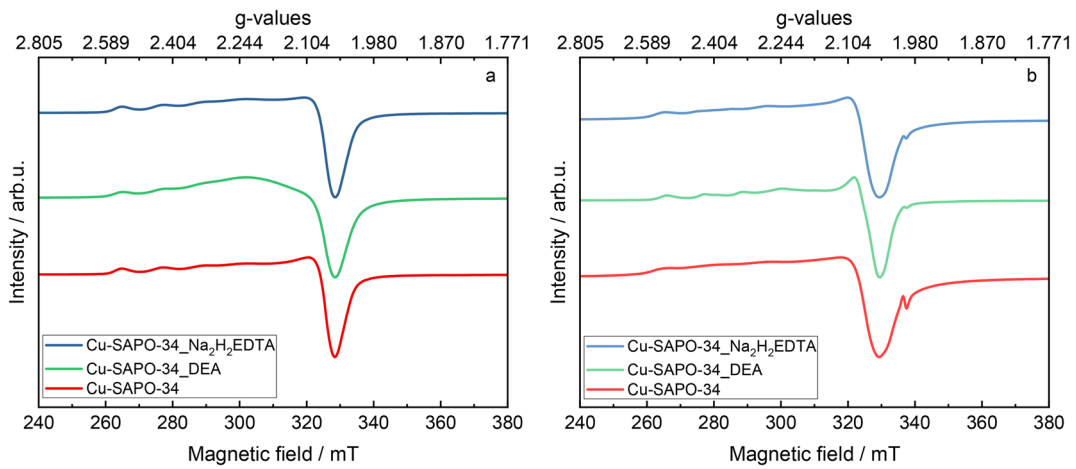

Fig. 10 a) EPR spectra of Cu-containing SAPO-34 samples recorded at room temperature (*ca.* 25 °C), and b) (activated at 200 °C for 2 h under vacuum) recorded at −196 °C.

paramagnetic ion and of the Cu hyperfine interaction (hfi) tensor A describing the magnetic interaction between the unpaired electron and the copper nucleus. These spin Hamiltonian parameters contain detailed information about the structural properties of Cu^{2+} species as they depend on the local coordination geometry of the cupric ion and therefore on the type and structure of the cation site in the framework of the material. The latter is influenced by multiple factors such as the zeolite structure, distribution and ratio of n(Si)/n(Al), copper content, synthesis techniques, post-synthesis treatments, and methods for copper incorporation.[7,44,58–60] In the case of ion-exchanged SAPO-34, the Cu^{2+} spin Hamiltonian parameters reported for the hydrated (calcined at 550 °C for 4 h in static air) and dehydrated materials have been assigned to specific cation positions based on continuous wave (CW) EPR experiments in combination with pulsed EPR spectroscopy[61] and quantum chemical computations.[62] Fig. 10a displays the EPR spectra of the hydrated samples recorded at room temperature (*ca.* 25 °C) chosen to distinguish between rigid and mobile species. The three samples exhibit a superposition of the typical anisotropic signal of one rigid Cu^{2+} species (species A) with spin Hamiltonian parameters ($g_{xx,yy}$ = 2.063, g_{zz} = 2.370, $A_{xx,yy}$ = 30 MHz, A_{zz} = 417 MHz) and an approximately isotropic signal of a minor mobile Cu^{2+} species B with a g_{iso} = 2.13. Species B is in particular present for Cu-SAPO-34_DEA.

The relative amount of paramagnetic Cu^{2+} species in the hydrated samples has been determined by double integration of their EPR spectra.[44,58] For direct comparison, the relative EPR intensity of the Cu^{2+} signal was normalized with the weight of the respective sample. The relative EPR intensity of Cu-SAPO-34_DEA is approximately four times higher than that of Cu-SAPO-34 and two times higher than that of Cu-SAPO-34_Na_2H_2EDTA (Table 3). This trend is in very good agreement with elemental analysis using ICP-OES.

Even though the EPR intensity for all the samples decreases by at least 50% after dehydration, hyperfine splitting of Cu with broadened shoulders occurred at the parallel region which indicates that more than one species is present. At least three distinct species have been identified (species C, D, and E; a summary of their parameters is given in Table 4) by spectral simulations provided in Fig. 11, while their respective weight contribution in the spectra is summarized in Table 3. Cu-SAPO-34 contains predominantly species D (g_{zz} ~2.338 and A_{zz} ~475 MHz) with 65% weight and species C (g_{zz} = 2.380 and A_{zz} = 386 MHz) also present with 35% weight. However, for Cu-SAPO-34_DEA, species C is the major component with 65% followed by species D and species E (g_{zz} = 2.398 and A_{zz} = 355 MHz) with 30% and 5%, respectively. Lastly, in Cu-SAPO-34_ Na_2H_2EDTA, Cu speciation is dominated by species E (60%).

Spin Hamiltonian parameters for species A are typical for an isolated Cu^{2+} species with octahedral coordination and according to previous studies can be assigned as $Cu(II)(O_f)_3(H_2O)_3$ at site I (*i.e.*, displaced from the six-ring into the ellipsoidal cavity; site assignments according to ref. 61 and 62), where O_f refers to the framework oxygen near the plane of the six-membered ring on the zeolite network.[58,59,61] In Fig. 10a, the anisotropic pattern of species A is dominant at room temperature for all the samples supporting the fact that the majority of Cu cations are bound to framework oxygen atoms with additional water molecules coordinating to the metal ions. A minor part of the cupric ions (species B) are presumably present as $Cu(II)(H_2O)_6$ complexes undergoing a fast tumbling motion at room temperature.[58] Upon the dehydration of the Cu-containing SAPO-34, it is suggested that Cu^{2+} cations have less interaction with water molecules hence strengthening their interaction with the oxygen atoms from the zeolite framework.[60] From the pulse EPR approach by Zamadics *et al.*,[61] species C corresponds to the Cu species with a connection to four oxygen frameworks and one water molecule $Cu(II)(O_f)_4(H_2O)$ which is probably situated near the center of the ellipsoidal cavity (site II). The computational point of view from Fernández *et al.*[62] added one possibility that species C might be situated at the center of the hexagonal prism (site III) to have a stable geometrical position. Species D (g_{zz} = 2.338 and A_{zz} = 475 MHz) can be assigned to site I although the g_{zz} value in our current study (g_{zz} ~2.338) is appreciably higher than the computational approach (g_{zz} between 2.230–2.240).[62] In addition, species E (g_{zz} = 2.398 and A_{zz} = 355 MHz) might be correlated to the presence of Cu hydroxyl complexes $Cu(II)(OH^-)_m$ or $Cu(II)(O_f)_n(OH^-)_m$ characterized by its hyperfine tensor around 350 MHz.[62] However, it should be noted that the g_{zz} value is also higher than the computational approach (g_{zz} ~2.231) probably due to the higher coordination number of cupric ions (*e.g.*, six-fold or five-fold instead of four-fold coordination).

Table 3 Relative EPR intensity obtained from experimental spectra of hydrated (calcined at 550 °C for 4 h in static air) Cu-containing SAPO-34, and composition in percentage for different Cu species in activated (200 °C for 2 h under vacuum) Cu-containing SAPO-34 samples obtained from the spectral simulations using EasySpin[28] (*the uncertainty of 3% has been estimated during spectral simulation)

Samples	Relative EPR intensity	C/%	D/%	E/%
Cu-SAPO-34	1.0	25	65	10
Cu-SAPO-34_DEA	4.0	65	30	5
Cu-SAPO-34_Na_2H_2EDTA	1.9	10	30	60

3.3 Investigation of the reaction

Fig. 12 reports NO adsorption IR experiments on O_2 activated samples. The presented spectra refer to the saturation of all accessible copper sites with NO. The absence of the band centred at 1810 cm^{-1} due to the ligation of NO to isolated Cu^+ – thus the formation of Cu^+(NO) mononitrosyls – is a distinctive feature of the materials studied.[63] It proves that the copper ions in the SAPO-34 catalysts are present solely in the form of copper(II) moieties and/or the existing copper(I) cations are inaccessible to NO, if any. The Cu^{2+}(NO)

Table 4 Spin Hamiltonian parameters used for spectral simulation of Cu-containing SAPO-34 after activation (200 °C for 2 h under vacuum)

Cu species	$g_{xx,yy}$	g_{zz}	$A_{xx,yy}$/MHz	A_{zz}/MHz	lwpp/mT	Assignment
A	2.063 ± 0.005	2.370 ± 0.005	30 ± 10	417 ± 5	3.0 ± 0.3	Cu(II)$(O_f)_3(H_2O)_3$ (site I)
B	2.130[a]	—	—	—	5.0 ± 0.3	Cu(II)$(H_2O)_6$
C	2.063 ± 0.005	2.380 ± 0.005	30 ± 10	386 ± 5	3.0 ± 0.3	Cu(II)$(O_f)_4(H_2O)$ (site II) or site III
D	2.067 ± 0.005	2.338 ± 0.005	30 ± 10	475 ± 5	3.0 ± 0.3	Site I
E	2.063 ± 0.005	2.398 ± 0.005	30 ± 10	355 ± 5	3.0 ± 0.3	Cu(II)$(OH^-)_m$ or Cu(II)$(O_f)_n(OH^-)_m$

[a] g_{iso} is an isotropic g-value.

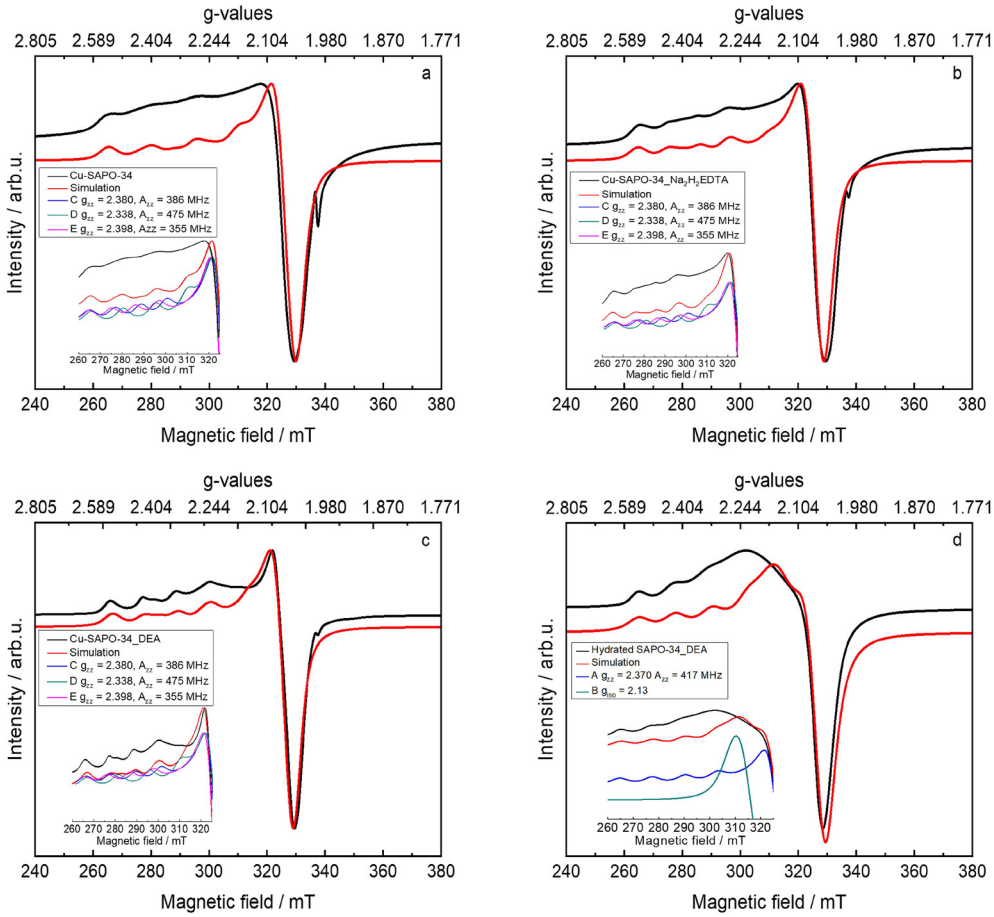

Fig. 11 Experimental (black) and simulated (red) EPR spectra of the activated samples a) Cu-SAPO-34, b) Cu-SAPO-34_Na_2H_2EDTA, and c) Cu-SAPO-34_DEA, recorded at −196 °C, and d) EPR spectra of the hydrated Cu-SAPO-34_DEA recorded at room temperature (*ca.* 25 °C). The insets show the contributions from different Cu species to the simulations.

mononitrosyls are detected in the 1950–1890 cm^{-1} range. The heterogeneous nature of Cu^{2+} cations reflects their various locations in the SAPO-34 structure. The location of isolated Cu^{2+} ions either in the 6MR units or in the 8MR positions of the chabazite cavity has been defined according to DFT data and validated in the experimental IR spectra with IR bands between 1907 and 1950 cm^{-1}.[40] Similarly, in Cu-SAPO-34, the 1920 and 1943 cm^{-1} bands are associated with NO bonded to Cu^{2+} in 6MRs and 8MRs, respectively. The band observed at 1890 cm^{-1} in the IR spectra of Cu-SAPO-34_DEA as the dominant species is assigned either to dimeric $[Cu–O–Cu]^{2+}$ species or to $Cu^{2+}(OH)$ sites located in six-membered rings. By analogy, the 1903 cm^{-1} band can originate from mononitrosyls formed by $Cu^{2+}(OH)$ located in eight-membered rings. It is shown that the contribution of respective copper(II) species depends on the post-modification of SAPO-34. The developed meso-/macropore surface promotes not only the accumulation of a greater number of Cu sites, but also the privileged formation of the $[Cu–O–Cu]^{2+}$ and $Cu^{2+}(OH)$ forms.

Upon contact with O_2 at 150 °C, the mononitrosyls and gaseous NO (1875 cm^{-1}) are transformed into nitrates species which are stabilized on Cu^{2+} sites, *i.e.*, $Cu^{2+}(NO_3^-)$.[41] In the experiment reported in Fig. 12b, the formation of nitrate

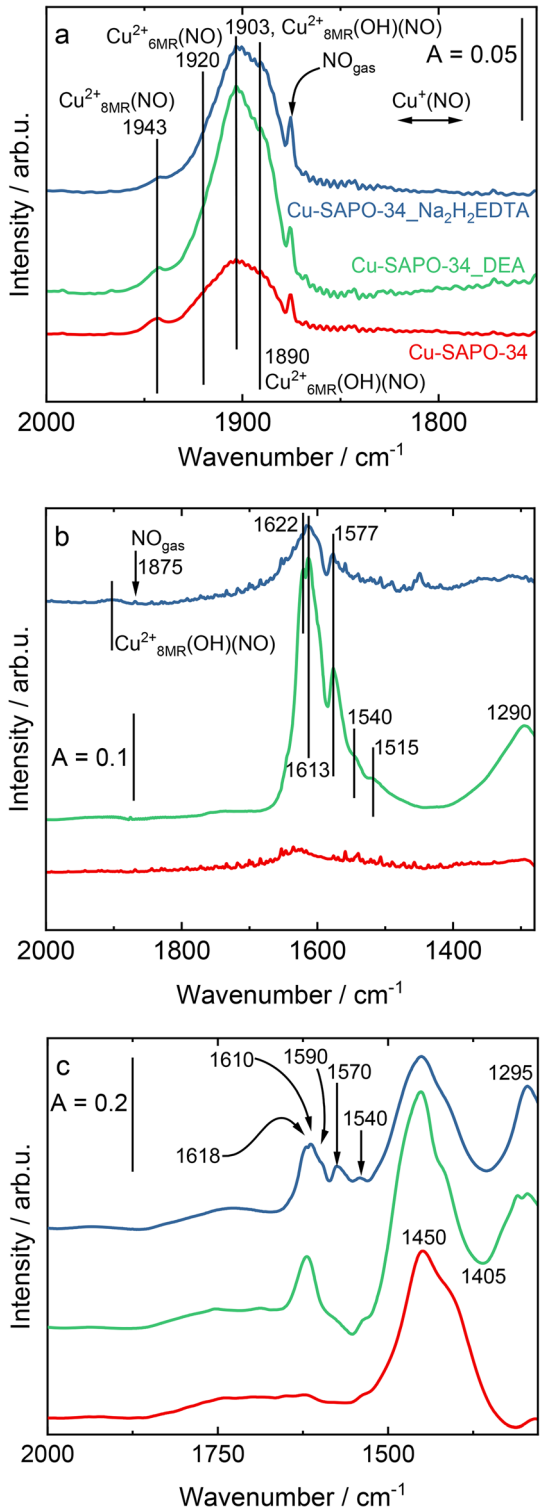

Fig. 12 The IR spectra of mononitrosyl species collected a) upon saturation of Cu-containing SAPO-34 with NO at room temperature (*ca.* 25 °C), b) in the N═O frequency range upon saturation of the catalysts with NO, a subsequent introduction of O_2 (stoichiometric for the NH_3-SCR-DeNO$_x$) and heating to 150 °C, and c) upon contact of nitrates with NH_3 at 150 °C for 10 min and subsequent cooling down to room temperature (*ca.* 25 °C).

species is confirmed by the appearance of 1622 and 1570–1515 cm^{-1} maxima in Cu-SAPO-34_DEA to the highest extent. In Cu-SAPO-34 free of intracrystalline mesoporosity, the conversion of NO and O_2 is negligible which can be ascribed to a low population of dimeric $[Cu–O–Cu]^{2+}$ species or to Cu^{2+}(OH) sites responsible for low-temperature SCR activity. The addition of NH_3 over the catalysts (Fig. 12c) covered with nitrate species (Fig. 12b) results in the elimination of the latter species from the catalyst surface. Thus, the dominating species are NH_4^+ ions (the bands centred at *ca.* 1450 cm^{-1}). The formation of water is documented by the band at 1618 cm^{-1} visible for the most active Cu-SAPO-34_DEA. The high abundance of NH_4^+ can suggest that NH_3 stored on Cu^{2+} sites is more reactive towards nitrates than NH_3 stored on Brønsted sites, being consumed at higher temperatures or at a prolonged time when the migration of ammonia molecules from Brønsted sites to Cu sites is expected.

Fig. 13 shows the results of catalytic data without and with the presence of 5 vol% H_2O. It can be seen that for NH_3-SCR-DeNO$_x$ without H_2O (Fig. 13a), Cu-SAPO-34_DEA exhibits the highest NO conversion below 250 °C, and the widest activity

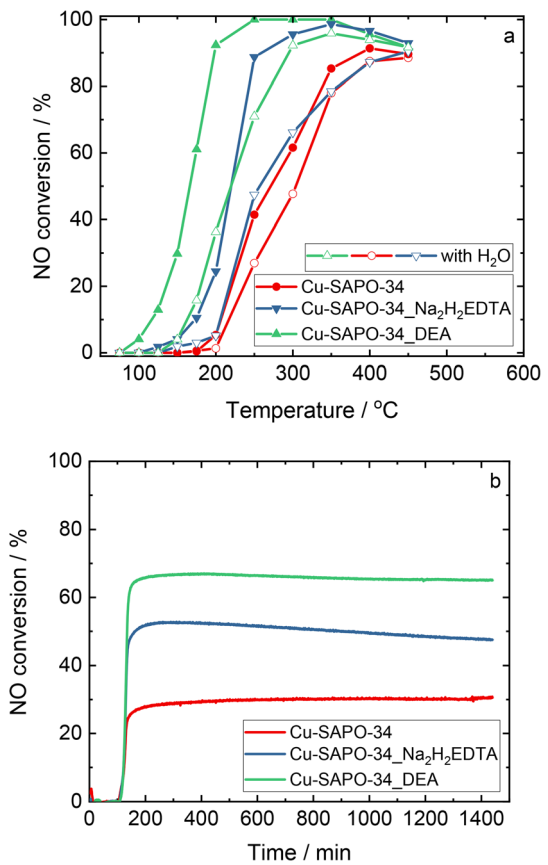

Fig. 13 Results of catalytic studies: a) NO conversion, reaction conditions: m_K = 0.2 g, F_{TOT} = 120 ml min^{-1}, c(NO) = 500 ppm, c(NH_3) = 575 ppm, c(O_2) = 4 vol%, (c(H_2O) = 5 vol% when used), He balance, GHSV = 30 000 h^{-1}, and b) time-on-stream at 250 °C, reaction conditions: m_K = 0.2 g, F_{TOT} = 120 ml min^{-1}, c(NO) = 500 ppm, c(NH_3) = 575 ppm, c(O_2) = 4 vol%, c(H_2O) = 5 vol%, He balance, GHSV = 30 000 h^{-1}.

temperature window to achieve more than 80% of NO conversion (200–450 °C). Meanwhile, the NO conversion for Cu-SAPO-34_Na_2H_2EDTA and Cu-SAPO-34 was significantly lower. N_2O was not detected for all investigated catalysts both with and without H_2O. The NO conversion significantly decreased for the catalytic tests in the presence of H_2O, which is especially pronounced for Cu-SAPO-34_Na_2H_2EDTA and Cu-SAPO-34 (Fig. 13a). The stability time-on-stream tests at 250 °C in the presence of H_2O revealed the stability of Cu-SAPO-34 and Cu-SAPO-34_DEA. Otherwise, the NO conversion for Cu-SAPO-34_Na_2H_2EDTA successively goes down (Fig. 13b). This effect can be ascribed to the migration of copper species inside of zeolite grains, and thus, lower accessibility of the reactant to the catalytically active sites. Furthermore, this statement can be supported by the *in situ* XPS data, where we observe a stronger decrease of n(Cu)/n(Al) ratio with increasing temperature (and time) under vacuum. For the micro-/mesoporous Cu-containing SAPO-34 reported in the literature, the NO conversion of above 80% was achieved in the range of 150–500 °C without H_2O in the feed (175–500 °C with H_2O in the feed).[12–15] Other authors reported also minor N_2O formation over micro-/mesoporous Cu-containing SAPO-34 below 25 ppm,[12,13] including extremely low N_2O concentration (below 5 ppm).[64] The time-on-stream tests approve the stability of micro-/mesoporous catalysts even when 5–10 vol% of H_2O was introduced.[13,14] Furthermore, previous studies over micro-/mesoporous Cu-containing SAPO-34 investigated in NH_3-SCR-DeNO$_x$ revealed that the formed mesopores improved the accessibility of reactants to catalytically active sites in the microporous channels.[12,14,15,65] Contrary to that our previous studies concerning micro-/mesoporous Cu-ZSM-5 and Cu–Y revealed that the mesopores introduced into Cu-containing zeolite catalysts do not play any direct role in the activity on NH_3-SCR-DeNO$_x$.[31,33] Instead, we observed that the applied post-modifications resulted in the introduction by ion-exchange of a higher amount of copper species, resulting in enhanced activity in NH_3-SCR-DeNO$_x$. Also, in the case of post-modified SAPO-34 with Na_2H_2EDTA or DEA, a higher amount of copper species is introduced. We did not observe any NO conversion for pure SAPO-34 (calcined at 550 °C for 4 h in static air) both without and with water vapor in the feed.

Accumulating the spectra in standard mode allows for detecting the stable species, however, without the proper insight into the reaction path. By employing the rapid scan approach, which allowed us to collect one spectrum within 0.3 s the consecutive reaction steps were identified in the first 300 s of NH_3-SCR-DeNO$_x$ in the presence of H_2O (Fig. 14). The contact of mesopore free Cu-SAPO-34 with SCR reagents at 150 °C leads to saturation of the copper(II) sites with bidentate and bridging NO_3^- species, as manifested by 1624 and 1280 cm^{-1} bands' evolution (Fig. 14a). The NO_3^- species were formed within the first 30 s of NH_3-SCR-DeNO$_x$ then no changes in their concentration were detected. In the presence of Cu-SAPO-34_Na_2H_2EDTA the appearance of the NO_3^- species is spread over time and

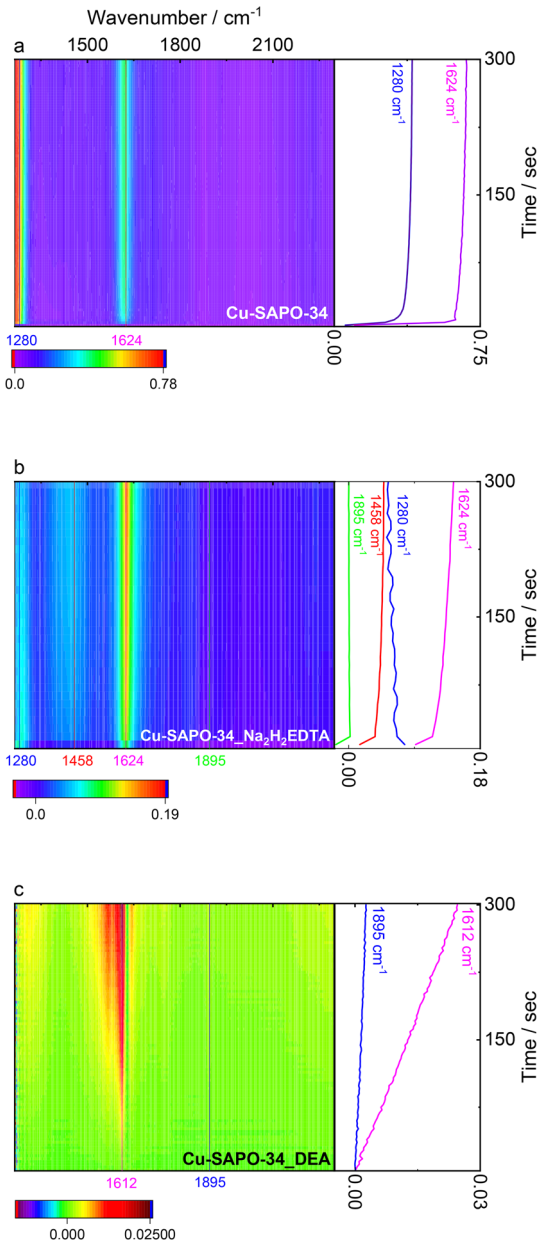

Fig. 14 Time-dependent contour maps of FT-IR difference spectra recorded in rapid scan mode and the time profiles of the respective intermediates gathered on the catalyst surface during the first 300 s of NH_3-SCR-DeNO$_x$ carried out at 150 °C, a) Cu-SAPO-34, b) Cu-SAPO-34_Na_2H_2EDTA, and c) Cu-SAPO-34_DEA.

accompanied by NH_4^+ band evolution which evidences that NH_3-SCR-DeNO$_x$ was launched in the presence of this material (Fig. 14b). The spectra of Cu-SAPO-34_DEA are the least abundant in surface species as the formation of water as the only moiety is documented by the 1612 cm^{-1} band. The evolution of this band starts immediately with the contact of reagents with the catalysts and any intermediates were not detected suggesting that their half-life time is short enough to not be detected even within 0.1–0.3 s (Fig. 14c). Thus, the high catalytic activity of Cu-SAPO-34_DEA is reported.

4. Conclusions

Micro-/meso-/macroporous Cu-containing SAPO-34 was prepared by the treatment of the support with an aqueous solution of DEA. The treatment with a solution of Na_2H_2EDTA was not effective for the introduction of mesopores. Subsequently, the modification of the support allows for the introduction of a higher amount of copper species (1.0–2.6 wt% compared to 0.5 wt% of Cu for the conventional Cu-SAPO-34). The micro-/meso-/macroporous Cu-SAPO-34_DEA reveals enhanced NO conversion compared to Cu-SAPO-34 or Cu-SAPO-34_Na_2H_2EDTA, due to the presence of dimeric $[Cu–O–Cu]^{2+}$ species and $Cu^{2+}(OH)$ sites responsible for low-temperature SCR activity. The role of formed meso-/macropores in the overcoming of diffusion limitations in NH_3-SCR-DeNO$_x$ was not excluded. The insight into the reaction *via* the rapid scan FT-IR approach evidenced the formation of the NO_3^- and NH_4^+ species that launched NH_3-SCR-DeNO$_x$.

Author contributions

Magdalena Jabłońska: conceptualization, methodology, investigation, data curation, writing – original draft, writing – review & editing, supervision. Kinga Góra-Marek: investigation, data curation, writing – review & editing. Muhammad Fernadi Lukman: investigation, data curation, writing – review & editing. Karolina Tarach: investigation, data curation. Konstantin Marcinowski: investigation. David Poppitz: investigation, data curation. Marko Bertmer **https://sciprofiles.com/profile/author/WHR3QVBzRkFaWHJUMTJzMWNGSU9nVkJLMXowTmk3c0ZY-NTNXZk16M3RXaz0=**: investigation, data curation. Reinhard Denecke: investigation, data curation, review. Andreas Pöppl: review. Roger Gläser: review.

Conflicts of interest

There are no conflicts to declare.

Acknowledgements

M. J. acknowledges a DFG Research Grant JA 2998/2-1. K. M. acknowledges Erasmus+ Programme. M. F. L. acknowledges a DFG Research Grant of GRK:2721. The *in situ* FT-IR and DR UV-vis investigations were financed by Grant No. 2021/41/B/ST4/00048 from the National Science Centre, Poland. R. D. acknowledges the contributions of Dennis El Mouzawak in XPS investigations. For the purpose of Open Access, the author has applied a CC-BY public copyright licence to any Author Accepted Manuscript (AAM) version arising from this submission.

References

1 X. Li, J. Li, Y. Peng, H. Chang, T. Zhang, S. Zhao, W. Si and J. Hao, *Appl. Catal., B*, 2016, **184**, 246–257.
2 S. Wang, C. Fan, Z. Zhao, Q. Liu, G. Xu, M. Wu, J. Chen and J. Li, *Appl. Catal., A*, 2020, **597**, 117554.
3 C. Gao, J.-W. Shi, Z. Fan, B. Wang, Y. Wang, C. He, X. Wang, J. Li and C. Niu, *Appl. Catal., A*, 2018, **564**, 102–112.
4 J. H. Kwak, R. G. Tonkyn, D. H. Kim, J. Szanyi and C. H. F. Peden, *J. Catal.*, 2010, **275**, 187–190.
5 J.-S. McEwen, T. Anggara, W. F. Schneider, V. F. Kispersky, J. T. Miller, W. N. Delgass and F. H. Ribeiro, *Catal. Today*, 2012, **184**, 129–144.
6 D. W. Fickel and R. F. Lobo, *J. Phys. Chem. C*, 2010, **114**, 1633–1640.
7 F. Gao, E. D. Walter, N. M. Washton, J. Szanyi and C. H. F. Peden, *ACS Catal.*, 2013, **3**, 2083–2093.
8 D. W. Fickel, E. D'Addio, J. A. Lauterbach and R. F. Lobo, *Appl. Catal., B*, 2011, **102**, 441–448.
9 S. Zhang, L. Pang, Z. Chen, S. Ming, Y. Dong, Q. Liu, P. Liu, W. Cai and T. Li, *Appl. Catal., A*, 2020, 117855.
10 K. Leistner, O. Mihai, K. Wijayanti, A. Kumar, K. Kamasamudram, N. W. Currier, A. Yezerets and L. Olsson, *Catal. Today*, 2015, **258**, 49–55.
11 M. Jabłońska, *Mol. Catal.*, 2022, **518**, 112111.
12 J. Liu, F. Yu, J. Liu, L. Cui, Z. Zhao, Y. Wei and Q. Sun, *J. Environ. Sci.*, 2016, **48**, 45–58.
13 Y. Mi, G. Li, Y. Zheng, Y. Luo, W. Liu, Z. Li, D. Wu and H. Peng, *Microporous Mesoporous Mater.*, 2021, 111245.
14 P. Wang, Z. Li, X. Wang, Y. Tong, F. Yuan and Y. Zhu, *ChemCatChem*, 2020, **12**, 4871–4878.
15 R. Li, P. Wang, S. Ma, F. Yuan, Z. Li and Y. Zhu, *Chem. Eng. J.*, 2020, **379**, 122376.
16 M. Rutkowska, M. Duda, A. Kowalczyk and L. Chmielarz, *C. R. Chim.*, 2017, **20**, 850–859.
17 D. Verboekend, M. Milina and J. Pérez-Ramírez, *Chem. Mater.*, 2014, **26**, 4552–4562.
18 D. Verboekend, N. Nuttens, R. Locus, J. Van Aelst, P. Verolme, J. C. Groen, J. Pérez-Ramírez and B. F. Sels, *Chem. Soc. Rev.*, 2016, **45**, 3331–3352.
19 D. Verboekend and J. Pérez-Ramírez, *ChemSusChem*, 2014, **7**, 753–764.
20 N. Nuttens, D. Verboekend, A. Deneyer, J. Van Aelst and B. F. Sels, *ChemSusChem*, 2015, **8**, 1197–1205.
21 S. Fernandez, M. L. Ostraat and K. Zhang, *AIChE J.*, 2020, **66**, e16943.
22 A. Gola, B. Rebours, E. Milazzo, J. Lynch, E. Benazzi, S. Lacombe, L. Delevoye and C. Fernandez, *Microporous Mesoporous Mater.*, 2000, **40**, 73–83.
23 B. M. Lok, C. A. Messina, R. L. Patton, R. T. Gajek, T. R. Cannan and E. M. Flanigen, *J. Am. Chem. Soc.*, 1984, **106**, 6092–6093.
24 S. Zhang, J. Chen, Y. Meng, L. Pang, Y. Guo, Z. Luo, Y. Fang, Y. Dong, W. Cai and T. Li, *Appl. Surf. Sci.*, 2021, 151328.
25 D. Massiot, F. Fayon, M. Capron, I. King, S. Le Calvé, B. Alonso, J.-O. Durand, B. Bujoli, Z. Gan and G. Hoatson, *Magn. Reson. Chem.*, 2002, **40**, 70–76.
26 E. W. Washburn, *Phys. Rev.*, 1921, **17**, 273.
27 **https://www.unifit-software.de**.
28 S. Stoll and A. Schweiger, *J. Magn. Reson.*, 2006, **178**, 42–55.
29 C. J. Van Oers, K. Góra-Marek, B. Prelot, J. Datka, V. Meynen and P. Cool, *Langmuir*, 2014, **30**, 1880–1887.

30 C. J. Van Oers, K. Góra-Marek, K. Sadowska, M. Mertens, V. Meynen, J. Datka and P. Cool, *Chem. Eng. J.*, 2014, **237**, 372–379.
31 M. Jabłońska, K. Góra-Marek, M. Grilc, P. C. Bruzzese, D. Poppitz, K. Pyra, M. Liebau, A. Pöppl, B. Likozar and R. Gläser, *Catalysts*, 2021, **11**, 843.
32 M. Rutkowska, I. Pacia, S. Basąg, A. Kowalczyk, Z. Piwowarska, K. A. Duda Michałand Tarach, K. Góra-Marek, M. Michalik, U. Díaz and L. Chmielarz, *Microporous Mesoporous Mater.*, 2017, **246**, 193–206.
33 R. S. R. Suharbiansah, K. Pyra, M. Liebau, D. Poppitz, K. Góra-Marek, R. Gläser and M. Jabłońska, *Microporous Mesoporous Mater.*, 2022, **334**, 111793.
34 L. Yang, C. Wang, L. Zhang, W. Dai, Y. Chu, J. Xu, G. Wu, M. Gao, W. Liu, Z. Xu, P. Wang, N. Guan, M. Dyballa, M. Ye, F. Deng, W. Fan and L. Li, *Nat. Commun.*, 2021, **12**, 4661.
35 A. Buchholz, W. Wang, M. Xu, A. Arnold and M. Hunger, *J. Phys. Chem. B*, 2004, **108**, 3107–3113.
36 Y. Watanabe, A. Koiwai, H. Takeuchi, S.-A. Hyodo and S. Noda, *J. Catal.*, 1993, **143**, 430–436.
37 Z. Li, J. Martínez-Triguero, P. Concepción, J. Yu and A. Corma, *Phys. Chem. Chem. Phys.*, 2013, **15**, 14670–14680.
38 K. Kanehashi, T. Nemoto and K. Saito, *J. Non-Cryst. Solids*, 2007, **353**, 4227–4231.
39 Z. Yan, B. Chen and Y. Huang, *Solid State Nucl. Magn. Reson.*, 2009, **35**, 49–60.
40 P. Concepción, M. Boronat, R. Millan, M. Moliner and A. Corma, *Top. Catal.*, 2017, **60**, 1653–1663.
41 S. Bordiga, C. Lamberti, F. Bonino, A. Travert and F. Thibault-Starzyk, *Chem. Soc. Rev.*, 2015, **44**, 7262–7341.
42 Q. Huo, D. I. Margolese and G. D. Stucky, *Chem. Mater.*, 1996, **8**, 1147–1160.
43 L. Martins, R. P. S. Peguin, M. Wallau and E. A. Urquieta González, *Stud. Surf. Sci. Catal.*, 2004, **154**, 2475–2483.
44 A. Palčić, P. C. Bruzzese, K. Pyra, M. Bertmer, K. Góra-Marek, D. Poppitz, A. Pöppl, R. Gläser and M. Jabłońska, *Catalysts*, 2020, **10**, 506.
45 U. Deka, I. Lezcano-Gonzalez, S. J. Warrender, A. L. Picone, P. A. Wright, B. M. Weckhuysen and A. M. Beale, *Microporous Mesoporous Mater.*, 2013, **166**, 144–152.
46 M. Hartmann and L. Kevan, *Chem. Rev.*, 1999, **99**, 635–663.
47 Y. Wan, G. Yang, J. Xiang, X. Shen, D. Yang, Y. Chen, V. Rac, V. Rakic and X. Du, *Dalton Trans.*, 2020, **49**, 764–773.
48 G. Yang, J. Ran, X. Du, X. Wang, Y. Chen and L. Zhang, *Microporous Mesoporous Mater.*, 2018, **266**, 223–231.
49 G. Turnes Palomino, P. Fisicaro, S. Bordiga, A. Zecchina, E. Giamello and C. Lamberti, *J. Phys. Chem. B*, 2000, **104**, 4064–4073.
50 R. Kumashiro, Y. Kuroda and M. Nagao, *J. Phys. Chem. B*, 1999, **103**, 89–96.
51 N. Nücker, J. Fink, B. Renker, D. Ewert and C. Politis, *Z. Phys. B: Condens. Matter*, 1987, **67**, 9.
52 B. J. Reedy and N. J. Blackburn, *J. Am. Chem. Soc.*, 1994, **116**, 1924–1931.
53 E. Borfecchia, K. A. Lomachenko, F. Giordanino, H. Falsig, P. Beato, A. V. Soldatov, S. Bordiga and C. Lamberti, *Chem. Sci.*, 2015, **6**, 548–563.
54 Q. Ye, L. Wang and R. T. Yang, *Appl. Catal., A*, 2012, **427**, 24–34.
55 H. Wang, R. Xu, Y. Jin and R. Zhang, *Catal. Today*, 2019, **327**, 295–307.
56 L. Meda and G. F. Cerofolini, *Surf. Interface Anal.*, 2004, **36**, 756–759.
57 M. C. Biesinger, B. P. Payne, A. P. Grosvenor, L. W. M. Lau, A. R. Gerson and R. S. C. Smart, *Appl. Surf. Sci.*, 2011, **257**, 2717–2730.
58 A. Godiksen, F. N. Stappen, P. N. R. Vennestrøm, F. Giordanino, S. B. Rasmussen, L. F. Lundegaard and S. Mossin, *J. Phys. Chem. C*, 2014, **118**, 23126–23138.
59 M. Urrutxua, B. Pereda-Ayo, U. De-La-Torre and J. R. González-Velasco, *ACS Omega*, 2019, **4**, 14699–14713.
60 J. Wang, D. Fan, T. Yu, J. Wang, T. Hao, X. Hu, M. Shen and W. Li, *J. Catal.*, 2015, **322**, 84–90.
61 M. Zamadics, X. Chen and L. Kevan, *J. Phys. Chem.*, 1992, **96**, 5488–5491.
62 E. Fernández, M. Moreno-González, M. Moliner, T. Blasco, M. Boronat and A. Corma, *Top. Catal.*, 2018, **61**, 810–832.
63 K. Góra-Marek, A. E. Palomares, A. Glanowska, K. Sadowska and J. Datka, *Microporous Mesoporous Mater.*, 2012, **162**, 175–180.
64 H. Xu, C. Lin, Q. Lin, X. Feng, Z. Zhang, Y. Wang and Y. Chen, *J. Environ. Chem. Eng.*, 2020, **8**, 104559.
65 L. Jin, X. Liu, C. Bian, J. Sheng, Y. Song and Y. Zhu, *Chin. Chem. Lett.*, 2020, **31**, 2137–2141.